

# $\alpha$ -Helix Peptide Folding and Unfolding Activation Barriers: A Nanosecond UV Resonance Raman Study

Igor K. Lednev, Anton S. Karnoup, Mark C. Sparrow, and Sanford A. Asher\*

Contribution from the Department of Chemistry, University of Pittsburgh, Pittsburgh, Pennsylvania 15260

Received April 27, 1999

**Abstract:** We used UV resonance Raman spectroscopy to characterize the equilibrium conformation and the kinetics of thermal denaturation of a 21 amino acid, mainly alanine,  $\alpha$ -helical peptide (AP). The 204-nm UV resonance Raman spectra show selective enhancements of the amide vibrations, whose intensities and frequencies strongly depend on the peptide secondary structure. These AP Raman spectra were accurately modeled by a linear combination of the temperature-dependent Raman spectra of the pure random coil and the pure  $\alpha$ -helix conformations; this demonstrates that the AP helix–coil equilibrium is well-described by a two-state model. We constructed a new transient UV resonance Raman spectrometer and developed the necessary methodologies to measure the nanosecond relaxation of AP following a 3-ns *T*-jump. We obtained the *T*-jump by using a 1.9- $\mu$ m IR pulse that heats the solvent water. We probed the AP relaxation using delayed 204-nm excitation pulses which excite the Raman spectra of the amide backbone vibrations. We observe little AP structural changes within the first 40 ns, after which the  $\alpha$ -helix starts unfolding. We determined the temperature dependence of the folding and unfolding rates and found that the *unfolding* rate constants show Arrhenius-type behavior with an apparent  $\sim 8$  kcal/mol activation barrier and a reciprocal rate constant of  $240 \pm 60$  ns at 37 °C. However, the *folding* rate constants show a negative activation barrier, indicating a failure of transition-state theory in the simple two-state modeling of AP thermal unfolding, which assumes a temperature-independent potential energy profile along the reaction coordinate. Our measurements of the initial steps in the  $\alpha$ -helical structure evolution support recent protein folding landscape and funnel theories; our temperature-dependent rate constants sense the energy landscape complexity at the earliest stages of folding and unfolding.

## Introduction

A protein's biological function is determined by its three-dimensional structure.<sup>1</sup> Since the majority of native protein structures self-assemble, these three-dimensional structures must be encoded by the proteins' primary sequences.<sup>1–6</sup> The major challenge in enzymology today is to elucidate this encoding mechanism, to develop decoding methods to directly predict a protein's structure from its primary sequence.

Despite the decades of studies of protein folding mechanism(s), it is still impossible to predict a protein's secondary and/or tertiary structure from its primary sequence.<sup>6</sup> Prediction of native protein structure has become more urgent due to the imminent completion of the sequencing of the human genome. It will soon be possible to empirically correlate disease with primary sequence mutations. Unfortunately, it is unlikely that identification of a protein mutation will give insight into the molecular origin of a disease since less than  $\sim 1\%$  of human proteins have

been well-characterized. The ability to predict structure and function of normal and mutated proteins from their primary sequences could lead to molecular strategies to alleviate human disease.

The encoding rules must be complex since for most proteins the primary sequence will encode both the native static structure as well as the folding dynamics. These folding dynamics are likely to be complex, with different structural components appearing in different time scales. In fact, recent theoretical models propose complex energy landscapes, which serve to efficiently funnel the folding protein toward its native form(s).<sup>4,5,7–13</sup> Theoretical studies predict, for example, that  $\alpha$ -helix propagation occurs on subnanosecond time scales, while nucleation of secondary structure motifs occur on nanosecond time scales.<sup>14–16</sup> Recently, fluorescence and IR studies have begun to examine protein folding and unfolding in nanosecond

\* To whom correspondence should be addressed. Phone: 412-624-8570. Fax: 412-624-0588. E-mail: asher+@pitt.edu.

(1) Creighton, T. E., Ed. *Protein Folding*; W. H. Freeman: New York, 1992.

(2) (a) Baldwin, R. L. *Nature* **1990**, *346*, 409–410. (b) Kim, P. S.; Baldwin, R. L. *Annu. Rev. Biochem.* **1990**, *59*, 631–660. (c) Ptitsyn, O. B.; Bychkova, V. E.; Uversky, V. N. *Philos. Trans. R. Soc. London, Ser. B* **1995**, *348*, 35–41. (d) Chan, H. S.; Bromberg, S.; Dill, K. A. *Philos. Trans. R. Soc. London, Ser. B* **1995**, *348*, 61–70.

(3) Matthews, C. R. *Annu. Rev. Biochem.* **1993**, *62*, 653–683.

(4) Bryngelson, J. D.; Onuchic, J. N.; Socci, N. D.; Wolynes, P. G. *Proteins: Struct., Funct., Genet.* **1995**, *21*, 167–195.

(5) Thirumalai, D.; Woodson, S. A. *Acc. Chem. Res.* **1996**, *29*, 433–439.

(6) Pennisi, E. *Science* **1996**, *273*, 426–428.

(7) Dill, K. A.; Chan, H. S. *Nat. Struct. Biol.* **1997**, *4*, 10–19.

(8) Chan, H. S.; Dill, K. A. *Proteins: Struct., Funct., Genet.* **1998**, *30*, 2–33.

(9) Nymeyer, H.; García, A. E.; Onuchic, J. N. *Proc. Natl. Acad. Sci. U.S.A.* **1998**, *95*, 5921–5928, and references therein.

(10) Doyle, R.; Simons, K.; Qian, H.; Baker, D. *Proteins: Struct., Funct., Genet.* **1997**, *29*, 282–291.

(11) Wolynes, P. G.; Luthey-Schulten, Z.; Onuchic, J. N. *Chem. Biol.* **1996**, *3*, 425–432.

(12) Socci, N. D.; Onuchic, J. N.; Wolynes, P. G. *J. Chem. Phys.* **1996**, *104*, 5860–5868.

(13) (a) Panchenko, A. R.; Luthey-Schulten, Z.; Wolynes, P. G. *Proc. Natl. Acad. Sci. U.S.A.* **1996**, *93*, 2008–2013. (b) Frauenfelder, H.; Sligar, S. G.; Wolynes, P. G. *Science* **1991**, *254*, 1598–1603. (c) Gutin, A. M.; Abkevich, V. I.; Shakhnovich, E. I. *Proc. Natl. Acad. Sci. U.S.A.* **1995**, *92*, 1282–1286.

time scales.<sup>17–26</sup> The large body of earlier work has clearly established that tertiary structures form within microsecond to second time scales.<sup>27,28</sup>

Despite the complexity of the folding dynamics, many proteins and peptides appear to fold and unfold via simple two-state kinetics without significant accumulation of intermediates in the folding pathway.<sup>15,22,29–32</sup> The low concentrations of intermediates makes it difficult to experimentally probe mechanistically crucial intermediates and transition states.<sup>32</sup> These states can only be probed kinetically, since they are too transiently populated to be directly observed<sup>32</sup> in equilibrium.

Kinetic studies of protein folding must characterize the structure of transient intermediate states and their rate of evolution. The typical approaches transiently destabilize the equilibrium protein structure using external stimuli such as pH jumps, denaturant concentration changes, solvent changes, temperature jumps (*T*-jumps), heme photoexcitation, etc. The relaxation kinetics and the structural evolution are typically monitored by using techniques such as CD, NMR, UV–visible absorption spectroscopy, IR and Raman spectroscopy, etc.<sup>16,20,28,33</sup>

(14) (a) Schwarz, G. J. *Mol. Biol.* **1965**, *11*, 64–77. (b) Brooks, C. L., III. *J. Phys. Chem.* **1996**, *100*, 2546–2549. (c) Eaton, W. A.; Muñoz, V.; Thompson, P. A.; Chan, C.-K.; Hofrichter, J. *Curr. Opin. Struct. Biol.* **1997**, *7*, 10–14. (d) Rank, J. A.; Baker, D. *Protein Sci.* **1997**, *6*, 347–354.

(15) Hagen, S. J.; Hofrichter, J.; Szabo, A.; Eaton, W. A. *Proc. Natl. Acad. Sci. U.S.A.* **1996**, *93*, 11615–11617.

(16) Eaton, W. A.; Thompson, P. A.; Chan, C.-K.; Hagen, S. J.; Hofrichter, J. *Structure* **1996**, *4*, 1133–1139.

(17) Muñoz, V.; Henry, E. R.; Hofrichter, J.; Eaton, W. A. *Proc. Natl. Acad. Sci. U.S.A.* **1998**, *95*, 5872–5879.

(18) Muñoz, V.; Thompson, P. A.; Hofrichter, J.; Eaton, W. A. *Nature* **1997**, *390*, 196–199.

(19) Thompson, P. A.; Eaton, W. A.; Hofrichter, J. *Biochemistry* **1997**, *36*, 9200–9210.

(20) Hagen, S. J.; Hofrichter, J.; Eaton, W. A. *J. Phys. Chem. B* **1997**, *101*, 2352–2365.

(21) (a) Chan, C.-K.; Hofrichter, J.; Eaton, W. A. *Science* **1996**, *274*, 628–629. (b) Hagen, S. J.; Hofrichter, J.; Eaton, W. A. *J. Phys. Chem.* **1996**, *100*, 12008–12021. (c) Lu, H. S. M.; Volk, M.; Kholodenko, Y.; Gooding, E.; Hochstrasser, R. M.; DeGrado, W. F. *J. Am. Chem. Soc.* **1997**, *119*, 7173–7180. (d) Jones, C. M.; Henry, E. R.; Hu, Y.; Chan, C.-K.; Luck, S. D.; Bhuyan, A.; Roder, H.; Hofrichter, J.; Eaton, W. A. *Proc. Natl. Acad. Sci. U.S.A.* **1993**, *90*, 11860–11864. (e) Ballew, R. M.; Sabelko, J.; Reiner, C.; Gruebele, M. *Rev. Sci. Instrum.* **1996**, *67*, 3694–3699. (f) Nötting, B.; Golbik, R.; Fersht, A. R. *Proc. Natl. Acad. Sci. U.S.A.* **1995**, *92*, 10668–10672.

(22) Gilmanshin, R.; Williams, S.; Callender, R. H.; Woodruff, W. H.; Dyer, R. B. *Biochemistry* **1997**, *36*, 15006–15012.

(23) Williams, S.; Causgrove, T. P.; Gilmanshin, R.; Fang, K. S.; Callender, R. H.; Woodruff, W. H.; Dyer, R. B. *Biochemistry* **1996**, *35*, 691–697.

(24) Phillips, C. M.; Mizutani, Y.; Hochstrasser, R. M. *Proc. Natl. Acad. Sci. U.S.A.* **1995**, *92*, 7292–7296.

(25) Thompson, P. A. In *Techniques in Protein Chemistry VIII*; Marshak, D. R., Ed.; Academic Press: San Diego, 1997; pp 735–743.

(26) Ballew, R. M.; Sabelko, J.; Gruebele, M. *Proc. Natl. Acad. Sci. U.S.A.* **1996**, *93*, 5759–5764.

(27) (a) Guo, Z.; Thirumalai, D. *Biopolymers* **1995**, *36*, 83–102. (b) Roder, H.; Colón, W. *Curr. Opin. Struct. Biol.* **1997**, *7*, 15–28.

(28) Plaxco, K. W.; Dobson, C. M. *Curr. Opin. Struct. Biol.* **1996**, *6*, 630–636, and references therein.

(29) (a) Yi, Q.; Baker, D. *Protein Sci.* **1996**, *5*, 1060–1066. (b) Villegas, V.; Azuaga, A.; Catasús, L.; Reverter, D.; Mateo, P. L.; Avilés, F. X.; Serrano, L. *Biochemistry* **1995**, *34*, 15105–15110. (c) Viguera, A. R.; Martínez, J. C.; Filimonov, V. V.; Mateo, P. L.; Serrano, L. *Biochemistry* **1994**, *33*, 2142–2150. (d) Jackson, S. E.; Fersht, A. R. *Biochemistry* **1991**, *30*, 10428–10435.

(30) Scalley, M. L.; Yi, Q.; Gu, H.; McCormack, A.; Yates, J. R., III; Baker, D. *Biochemistry* **1997**, *36*, 3373–3382.

(31) Chen, E.; Lapko, V. N.; Song, P.-S.; Klinger, D. S. *Biochemistry* **1997**, *36*, 4903–4908.

(32) Fersht, A. R. *Curr. Opin. Struct. Biol.* **1997**, *7*, 3–9.

(33) (a) Kuwajima, K. In *Circular Dichroism and the Conformational Analysis of Biomolecules*; Fasman, G. D., Ed.; Plenum Press: New York, 1996; pp 159–181. (b) Dyson, H. J.; Wright, P. E. *Annu. Rev. Phys. Chem.* **1996**, *47*, 369–395. (c) Mines, G. A.; Pascher, T.; Lee, S. C.; Winkler, J. R.; Gray, H. B. *Chem. Biol.* **1996**, *3*, 491–497.

These methods are limited by the dead time associated with the stimuli or the time resolution of the monitoring techniques. Chemical stimuli such as pH jumps and denaturant concentration changes are limited by the time required for mixing; the fastest mixing technique has a dead time of  $\sim 20 \mu\text{s}$ .<sup>34</sup>

Much faster kinetics can be studied by using laser-induced *T*-jumps in small volumes (nanoliters).<sup>19,22–26</sup> The characteristic time for the heating pulse energy redistribution into a temperature increase is very fast ( $\sim 70 \text{ ps}$ ).<sup>24</sup> These relaxation processes have been studied by fluorescence<sup>19,25,26</sup> and infrared spectroscopy<sup>22–24</sup> to probe the protein and polypeptide secondary structure evolution during the resulting thermal denaturation initiated by the nanosecond to microsecond *T*-jumps. The fluorescence studies require a fluorescence probe, which can be either an existing aromatic amino acid residue, or an artificially attached luminescent fluorophore.

The information obtained from the fluorescence data is somewhat indirect because the fluorescence spectrum, lifetime, and quantum yield do not simply report on protein structure. IR spectral measurements, in principle, directly probe the polypeptide backbone secondary structure, but until now only the amide I region between  $\sim 1600$  and  $1700 \text{ cm}^{-1}$ <sup>22–24</sup> has been available to study peptide secondary structure. Despite these hurdles these recent transient *T*-jump fluorescence and IR pioneering studies have achieved breakthroughs in the understanding of the earliest stages in protein folding and unfolding.<sup>17–24,26</sup>

Our work presented here<sup>35</sup> demonstrates a powerful new nanosecond structural tool to studying protein folding and unfolding dynamics. This work extends the powerful technique of steady state UV resonance Raman spectroscopy (UVRS) to protein dynamical studies. We have recently argued that UVRS is the most powerful structural probe for characterizing dilute solution protein secondary structure.<sup>36,37</sup> UV excitation within the peptide backbone amide  $\pi \rightarrow \pi^*$  transitions results in the selective enhancement of numerous amide vibrations whose frequencies and intensities directly report upon the protein secondary structure.<sup>38</sup> In addition, excitation at  $\sim 230 \text{ nm}$  allows the study of tyrosine and tryptophan environments;<sup>39</sup> the tyr and trp Raman cross sections directly report on the solvent exposure of these residues.<sup>39</sup>

We report here the use of nanosecond kinetic UVRS to examine peptide folding and unfolding. A  $1.9\text{-}\mu\text{m}$  laser pulse *T*-jump is used to initiate the  $\alpha$ -helix  $\rightarrow$  random coil thermal transition of an alanine–arginine-based 21 amino acid residue peptide. A variably delayed 204-nm UV excitation pulse excites the UVRS which provides information on the nanosecond secondary structure evolution of the peptide.

## Experimental Section

**Materials and Sample Preparation.** The 21 amino acid peptide (AP) of composition  $\text{A}_5(\text{A}_3\text{RA})_3\text{A}$  was prepared ( $>95\%$  purity) at the Pittsburgh Cancer Institute by using the solid-phase peptide synthesis method. Tri- and pentaalanine ( $\text{A}_3$  and  $\text{A}_5$ ) obtained from Sigma

(34) (a) Yeh, S.-R.; Han, S. V.; Rousseau, D. L. *Acc. Chem. Res.* **1998**, *31*, 727–736. (b) Takahashi, S.; Yeh, S.-R.; Das, T. K.; Chan, C.-K.; Gottfried, D. S.; Rousseau, D. L. *Nat. Struct. Biol.* **1997**, *4*, 44–50. (c) Takahashi, S.; Ching, Y.; Wang, J.; Rousseau, D. L. *J. Biol. Chem.* **1995**, *270*, 8405–8407.

(35) Lednev, I. K.; Karnoup, A. S.; Sparrow, M. C.; Asher, S. A. *J. Am. Chem. Soc.* **1999**, *121*, 4076–4077.

(36) Chi, Z.; Asher, S. A. *Biochemistry* **1998**, *37*, 2865–2872.

(37) Chi, Z.; Chen, X. G.; Holtz, J. S. W.; Asher, S. A. *Biochemistry* **1998**, *37*, 2854–2864.

(38) Song, S.; Asher, S. A. *J. Am. Chem. Soc.* **1989**, *111*, 4295–4305.

(39) Chi, Z.; Asher, S. A. *J. Phys. Chem.* **1998**, *102B*, 9595–9602.

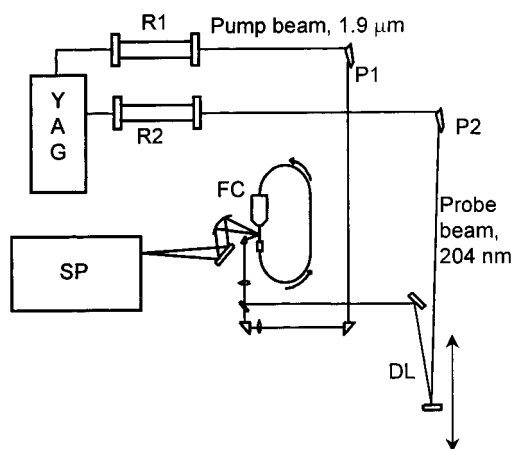


**Figure 1.** The *T*-jump spectrometer consists of a Nd:YAG laser (YAG), two H<sub>2</sub> Raman shifters (R1 and R2), a thermostated flow cell sample circulator (FC), and a Spex Triplemate triple monochromator with a blue enhanced ICCD detector (SP). The heating pump beam is obtained by Raman shifting the YAG fundamental in H<sub>2</sub> to 1.9  $\mu\text{m}$  (first Stokes). The probe beam is obtained by Raman shifting the YAG third harmonic to 204 nm (fifth anti-Stokes). The time delays between the pump and probe pulses are provided by the variable delay line (DL).

Chemical and trifluoroethanol (TFE) obtained from Aldrich were used as received.

***T*-Jump Raman Spectral Measurements.** The third harmonic of a Coherent Inc. Infinity YAG laser operating at 100 Hz with a 3.5-ns temporal pulse width was anti-Stokes Raman-shifted five harmonics in H<sub>2</sub> to 204 nm to excite the amide UVRS (Figure 1). At the 10- $\mu\text{J}$  excitation pulse energies used, we saw no evidence of nonlinear optical phenomena, Raman saturation,<sup>40,41</sup> or formation of amide *cis* species.<sup>42</sup> The Raman instrumentation used to collect, disperse, and detect the Raman scattered light has been described in detail elsewhere.<sup>42</sup>

To selectively heat the water solvent, we Raman-shifted the remaining part of the 1.06- $\mu\text{m}$  YAG fundamental ( $\sim 16$  mJ) to 1.9  $\mu\text{m}$  (1st H<sub>2</sub> Stokes shift) by using a 1-m Raman shifter (Light Age Inc.; 1000 psi H<sub>2</sub>) to obtain  $\sim 1.5$ -mJ pulse energies at our 100 Hz repetition rate. This 1.9- $\mu\text{m}$  excitation is absorbed by water overtones and the energy is thermalized in picoseconds by vibrational relaxation.<sup>24</sup>

We varied the delay time between the pump and probe pulses by changing their path length difference. The pump and probe beams were made collinear and were focused onto the sample with spot size diameters of  $\sim 300$   $\mu\text{m}$  (near-IR) and  $< 200$   $\mu\text{m}$  (UV).

We utilized a free surface temperature-controlled ( $\pm 0.5$   $^{\circ}\text{C}$ ) sample solution stream of  $\sim 0.6$ -mm diameter which circulated the sample through the laser beams. This free surface sample stream avoided problems such as interference from the Raman spectra of quartz windows, surface nonlinear optical phenomena and deposition on the windows of decomposition products. We utilized a 4  $^{\circ}\text{C}$  initial temperature for many of the measurements to minimize the shock wave induced by the incident IR heating pulse. This allowed us to utilize a maximum 65  $^{\circ}\text{C}$  *T*-jump, which was obtained by focusing the 1.5-mJ 1.9- $\mu\text{m}$  laser pulses to a  $\sim 300$ - $\mu\text{m}$  diameter in the flowing sample stream. Measurements in the absence of the pump pulse demonstrated that negligible sample heating occurs from the 10- $\mu\text{J}$  204-nm excitation pulse.

To ensure that the Raman signal was obtained from the sample volume maximally heated by the IR pulse we adjusted the sample absorbance at 204 nm to be sufficiently large such that the resonance Raman light collected originates mainly from the sample stream surface (Figure 2A). The water absorbance of 40/cm at 1.9  $\mu\text{m}$  decreases the IR beam intensity and the resulting *T*-jump 2.5-fold within the first

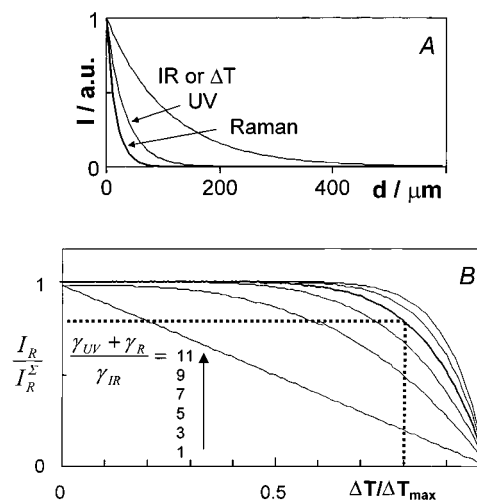


**Figure 2.** (A) Calculated sample depth intensity dependencies of incident 1.9- $\mu\text{m}$  pump beam and the 204-nm incident UV Raman excitation beam, given the sample absorbances at 1.9  $\mu\text{m}$  and 204 nm. Also shown is the calculated sample depth dependence for the collected 180° backscattered Raman intensity assuming identical absorbances at 204 nm and at the Raman scattered wavelength. (B) Fractional contribution of Raman scattering from the heated sample surface region calculated using eq 1 as a function of the parameter  $(\gamma_{\text{UV}} + \gamma_{\text{R}})/\gamma_{\text{IR}}$ .

100  $\mu\text{m}$  sample thickness. The fractional contribution of Raman signal,  $I_{\text{R}}/I_{\text{R}}^{\Sigma}$ , collected from the sample volume experiencing a *T*-jump between the maximum,  $\Delta T_{\text{max}}$  and a smaller  $\Delta T$  may be estimated from eq 1:

$$\frac{I_{\text{R}}}{I_{\text{R}}^{\Sigma}} \geq \left[ 1 - \left( \frac{\Delta T}{\Delta T_{\text{max}}} \right)^{(\gamma_{\text{UV}} + \gamma_{\text{R}})/\gamma_{\text{IR}}} \right] \quad (1)$$

where  $I_{\text{R}}$  is the Raman intensity collected from a sample volume which experiences a *T*-jump between  $\Delta T_{\text{max}}$  and  $\Delta T$  and  $I_{\text{R}}^{\Sigma}$  is the total Raman intensity collected.  $\gamma_{\text{UV}}$ ,  $\gamma_{\text{R}}$ , and  $\gamma_{\text{IR}}$  are the absorbances ( $\text{cm}^{-1}$ ) of the sample for the 204-nm excitation wavelength, for the Raman scattered wavelength and for the 1.9- $\mu\text{m}$  IR heating pulse, respectively. Equation 1 assumes only collection of 180° Raman backscattering. Thus, this expression underestimates the fraction of Raman scattering derived from the “hottest” volume of the sample.

Figure 2 illustrates the dependence of the fractional Raman scattering from the sample volume experiencing a *T*-jump between  $\Delta T_{\text{max}}$  and  $\Delta T$  upon the relative absorbances of the sample,  $(\gamma_{\text{UV}} + \gamma_{\text{R}})/\gamma_{\text{IR}}$ . For our *T*-jump experiments, we utilized 204-nm absorbances of  $\sim 150$   $\text{cm}^{-1}$  [ $(\gamma_{\text{UV}} + \gamma_{\text{R}})/\gamma_{\text{IR}} \approx 7$ ]. Thus,  $> 80\%$  of Raman scattering was collected from the sample volume experiencing a *T*-jump  $> 80\%$  of  $\Delta T_{\text{max}}$ .

We are developing a new transient Raman spectrometer which will utilize a  $\sim 1.5$ - $\mu\text{m}$  IR pump pulse which occurs in a region of smaller water absorption. This will allow us in the future to decrease the peptide concentration and to examine the concentration dependence of the folding/unfolding dynamics.

We independently verified the magnitude of the *T*-jump by measuring the pump beam energy dependence of the  $\sim 3400$   $\text{cm}^{-1}$  water Raman band. This band shows a large, well-known frequency and band shape temperature dependence.<sup>43</sup> We constructed a *T*-jump calibration curve (Figure 3) using our measured steady-state temperature spectral dependence (Figure 3B). We used the UVRR water difference spectrum in the presence versus absence of the pump beam (Figure 3C) and the measured calibration curve to determine the actual “average” *T*-jump in the probed volume.

**Absorption and CD Measurements.** We measured the near-IR, visible, and UV absorption spectra by using a Perkin-Elmer Lambda 9 absorption spectrometer. The CD spectra were measured by using a Jasco 710 spectropolarimeter. We calculated the temperature depen-

(40) Teraoka, J.; Harmon, P. A.; Asher, S. A. *J. Am. Chem. Soc.* **1990**, *112*, 2892–2900.

(41) Harmon, P. A.; Teraoka, J.; Asher, S. A. *J. Am. Chem. Soc.* **1990**, *112*, 8789–8799.

(42) Li, P.; Chen, X. G.; Shulin, E.; Asher, S. A. *J. Am. Chem. Soc.* **1997**, *119*, 1116–1120.

(43) Walrafen, G. E.; Fisher, M. R.; Hokmabadi, M. S.; Yang, W.-H. *J. Chem. Phys.* **1986**, *85*, 6970–6982.



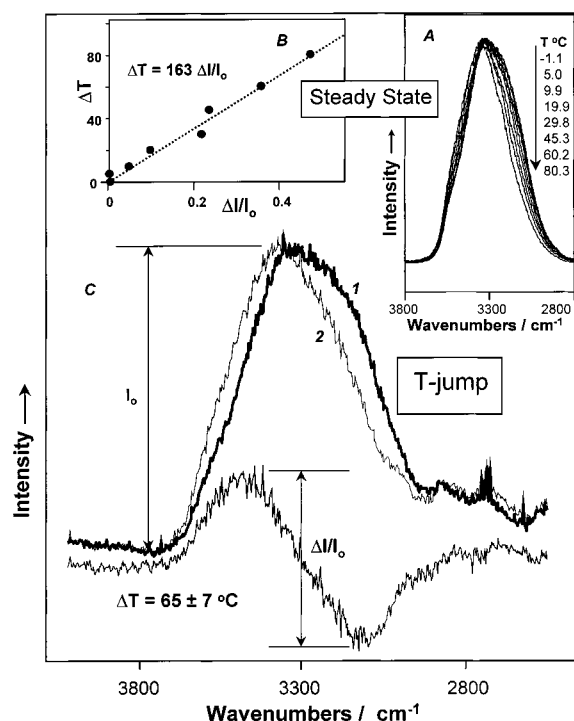


**Figure 3.** (A) Steady-state temperature dependence of the 204-nm UVRS of the O–H water stretching band at  $\sim 3400\text{ cm}^{-1}$ . (B)  $T$ -jump calibration curve which relates the magnitude of the O–H stretching peak spectral shift to the temperature change. The abscissa is the ratio of the peak to trough difference relative to the O–H stretching band peak intensity of the temperature difference spectra, as shown in part C. (C) UVRS of the O–H water stretching band measured (1) in the presence and (2) absence of the heating pulse. Also shown is the relative difference spectrum obtained by subtracting these spectra and ratioing the difference to the original spectrum. The measured value of  $\Delta I/I_0$  was used in conjunction with the calibration curve to determine the actual  $T$ -jump value.

dence of the AP secondary structure from the measured temperature dependence of the CD spectra by using eqs 2

$$[\theta(\lambda)]_{\text{obs}} = ([\theta(\lambda)]_{\alpha} - [\theta(\lambda)]_r)f_{\alpha} + [\theta(\lambda)]_r \quad (2a)$$

where  $[\theta(\lambda)]_{\text{obs}}$  are the observed 222-nm molar ellipticities per residue at each temperature and  $f_{\alpha}$  is the fractional  $\alpha$ -helical content.

The mean  $\alpha$ -helix molar ellipticity per residue for short  $\alpha$ -helical peptide may be estimated as<sup>44</sup>

$$[\theta]_n = [\theta]_{\infty}(n - k)/n \quad (2b)$$

where  $[\theta]_n$  and  $[\theta(\lambda = 222\text{ nm})]_{\infty} = -40\,000\text{ (deg cm}^2\text{)/dmol}$  are the mean residue ellipticity for a helix of  $n$  amides and for an infinite helix, respectively,<sup>45</sup> and  $k = 4.3$  is an empirically determined constant,<sup>44</sup> which takes into account the number of penultimate amino acid residues not involved in the  $\alpha$ -helix. Since AP has 21 amino acid sequence its  $\alpha$ -helical molar ellipticity at 222 nm is estimated via eq 2b to be  $-31\,400\text{ (deg cm}^2\text{)/dmol}$ . The estimated value is close to the values of  $[\theta(\lambda)]_{\alpha} = -32\,500$  and  $-32\,640\text{ (deg cm}^2\text{)/dmol}$  reported for the mean residue ellipticity averaged over several polypeptides<sup>46</sup> and proteins.<sup>47</sup> We determined a random coil molar ellipticity  $[\theta(\lambda = 222\text{ nm})]_r = -3200 \pm 600\text{ (deg cm}^2\text{)/dmol}$  (see Discussion) compared to previous

(44) Woody, R. W. In *Circular Dichroism and the Conformational Analysis of Biomolecules*; Fasman, G. D., Ed.; Plenum Press: New York, 1996; pp 25–67.

(45) Gans, P. J.; Lyu, P. C.; Manning, M. C.; Woody, R. W.; Kallenbach, N. R. *Biopolymers* **1991**, *31*, 1605–1614.

(46) Reed, J.; Reed, T. A. *Anal. Biochem.* **1997**, *254*, 36–40.

(47) Chen, Y.-H.; Yang, J. T.; Martinez, H. M. *Biochemistry* **1972**, *11*, 4120–4131.

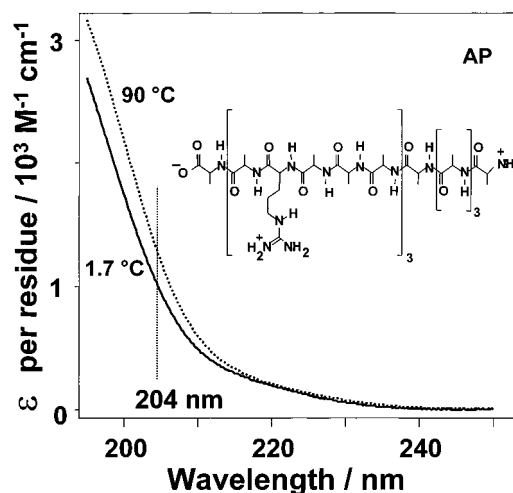


**Figure 4.** Absorption spectra of AP (0.5 mg/mL) at 1.7 and 90.5 °C. Inset: Molecular structure of AP.

estimates of  $-2340\text{ (deg cm}^2\text{)/dmol}$ .<sup>47</sup> Our modeling assumes temperature-independent molar ellipticities.

## Results

**Steady-State UV Absorption and CD Measurements.** The AP peptide studied here is very similar to a peptide first studied by Lockhart and Kim.<sup>48,49</sup> Their peptide, which had different terminal groups, was shown by CD and NMR to be predominantly  $\alpha$ -helical at 0 °C,<sup>48,49</sup> but melted noncooperatively as the temperature increased.

Figure 4 shows the absorption spectra of our AP peptide at  $T = 1.7$  and 90 °C. The increase in AP absorbance with temperature derives mainly from conversion of the  $\alpha$ -helix to the random coil, which results in hyperchromism due to the loss of  $\alpha$ -helix excitonic interactions.<sup>50</sup>

We used CD to monitor directly changes in the  $\alpha$ -helical content. Figure 5A shows the temperature dependence of the AP CD spectra (5.9 mg/mL), while Figure 5B shows the temperature dependence of  $[\theta(222\text{ nm})]_{\text{obs}}$  and Figure 5C shows our eq 2 calculated temperature dependence of the fraction of  $\alpha$ -helical content.

Our low-temperature AP CD spectra (Figure 5A) are similar to those found for  $\alpha$ -helical peptides with minima at 222 and 206 nm.<sup>44</sup> The low-temperature CD spectra of AP shows a 222-nm trough associated<sup>51</sup> with the existence of a substantial  $\alpha$ -helix content. The magnitude of this trough decreases as the temperature increases due to melting of the  $\alpha$ -helix.

Addition of  $\alpha$ -helical stabilizer TFE to the AP solution increases the 222-nm ellipticity as shown in the Figure 5A inset, and also increases the  $\alpha$ -helix melting temperature by  $\sim 40$  °C (Figure 5B). This dependence of the 222-nm AP ellipticity on TFE concentration (Figure 5A, inset) is similar to that reported for other A peptides.<sup>45,52</sup> We can use the low-temperature, high TFE concentration 222-nm molar ellipticity of AP to estimate

(48) Lockhart, D. J.; Kim, P. S. *Science* **1992**, *257*, 947–951.

(49) Lockhart, D. J.; Kim, P. S. *Science* **1993**, *260*, 198–202.

(50) (a) Gratzer, W. B. In *Poly- $\alpha$ -Amino Acids, Protein Models for Conformational Studies*; Fasman, G. D., Ed.; Marcel Dekker: New York, 1967; Chapter 5. (b) Robin, M. B. *Higher Excited States of Polyatomic Molecules*; Academic Press: New York, 1975; Vol. II, p 140. (c) Momii, R. K.; Urry, D. W. *Macromolecules* **1968**, *1*, 372. (d) Onari, S. *Jpn. J. Appl. Phys.* **1970**, *9*, 227.

(51) Kallenbach, N. R.; Lyu, P.; Zhou, H. In *Circular Dichroism and the Conformational Analysis of Biomolecules*; Fasman, G. D., Ed.; Plenum Press: New York, 1996; pp 201–259.

(52) Lyu, P. C.; Wang, P. C.; Liff, M. I.; Kallenbach, N. R. *J. Am. Chem. Soc.* **1991**, *113*, 3568–3572.

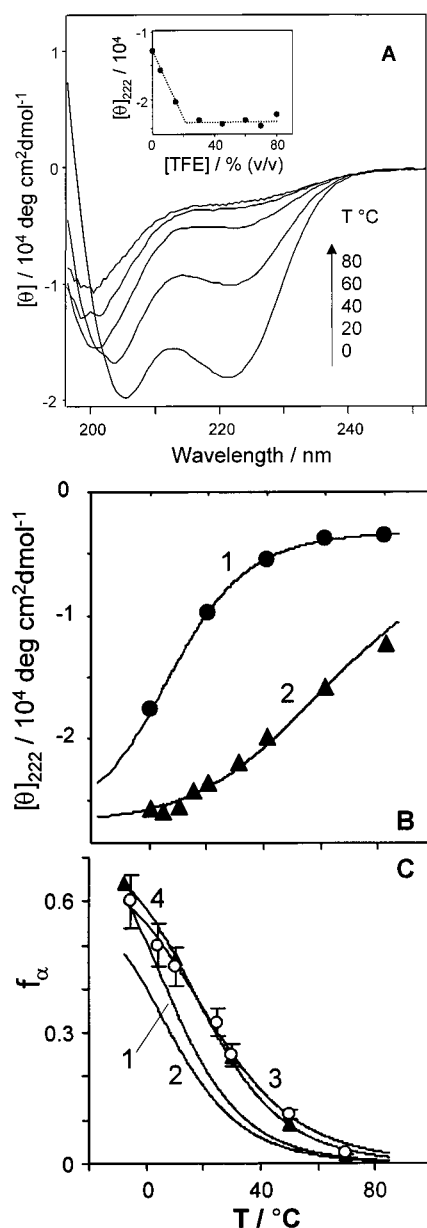


**Figure 5.** (A) Temperature dependence of aqueous solution CD spectra of AP (5.9 mg/mL). Also shown in the inset is the dependence of the AP 222-nm ellipticity as a function of TFE concentration measured at 15 °C. (B) The 222-nm CD melting curves of AP (5.9 mg/mL) (1) in water and (2) in a water–TFE mixture (45% V/V). The solid curves are the best fits to eq 7 of the measured temperature dependence of the 222-nm molar ellipticities.  $[\theta]_{\alpha}$  was determined to be  $-26\,000$  (deg  $\text{cm}^2$ )/dmol from the CD of AP in the presence of TFE. This fit also yields values of (1)  $[\theta]_{\text{r}} = -3200 \pm 600$  (deg  $\text{cm}^2$ )/dmol,  $\Delta H = -12.1 \pm 1$  kcal/mol, and  $\Delta S = -43.2 \pm 4$  cal/(mol K), with  $R^2 > 0.999$  for AP in pure water, and (2)  $\Delta H = -9 \pm 2$  kcal/mol, and  $\Delta S = -27 \pm 8$  cal/(mol K), with  $R^2 > 0.988$  for AP in the water–TFE solution. (C) Calculated temperature dependence of AP (5.9 mg/mL)  $\alpha$ -helical fraction,  $f_{\alpha}$  determined from CD measurements (curves 1 and 2) and UVRS measurements (curves 3 and 4). Curves 1 and 2 were calculated using eq 8 with thermodynamic parameters determined from the fits to curve 1 of Figure 5B. Curve 1 was calculated by using  $f_{\text{end}} = 0.215$ , while curve 2 was calculated by using  $f_{\text{end}} = 0.38$  (see text). Curves 3 and 4 show the UVRS calculated temperature dependence of the AP fractional  $\alpha$ -helix abundance (curve 3,  $\circ$ , 15 mg/mL; curve 4,  $\blacktriangle$ , 0.5 mg/mL). The solid lines through the data points are the best fits to thermodynamic model eq 8:  $f_{\text{end}}$  was determined to be  $0.32 \pm 0.1$  for the 15 mg/mL sample and  $0.29 \pm 0.06$ , for the 0.5 mg/mL sample. The thermodynamic parameters are listed in Table 2,  $R^2 \geq 0.994$  in both cases.

the ellipticity which would occur for 100%  $\alpha$ -helical AP, to obtain the value of  $[\theta(\lambda)]_{\alpha} = -26\,000 \pm 1000$  (deg  $\text{cm}^2$ )/dmol of eq 2a.<sup>45,52</sup>

This calculated value of  $[\theta(\lambda)]_{\alpha}$  is 19% smaller than the value  $[\theta(\lambda)]_{\alpha} = -32\,000 \pm 700$  (deg  $\text{cm}^2$ )/dmol reported for a capped 21-residue A-based peptide.<sup>45</sup> Our decreased value may reflect disorder at the uncapped AP termini. For AP we calculate a value of  $k = 7.6$  in eq 2b which has previously been reported to range between 4.6 and 6.3, because it strongly depends on  $\phi$  and  $\Psi$  values in the  $\alpha$ -helix.<sup>45</sup> The CD spectra are also dependent on the side chain identities.<sup>46</sup> The fully ordered helical form of poly-L-alanine has  $[\theta]_{\infty} = -31\,000$  (deg  $\text{cm}^2$ )/dmol.<sup>53</sup>

We also measured the temperature dependence of the AP CD spectra at higher concentrations to check whether any aggregation phenomena occur at the higher concentrations used for our transient Raman measurements and affect the  $\alpha$ -helix content. For our time-resolved experiments we require AP concentrations as high as 15 mg/mL (6.7 mM) to have sufficient absorbance in the UV to define our  $T$ -jump values. Neither the AP CD spectra nor the melting curves show a dependence over the concentrations required for the UV Raman studies. This is consistent with previous A-peptide studies, which found no evidence of aggregation, and found that the helix  $\rightarrow$  random coil thermal transition is independent of peptide concentration between 4  $\mu\text{M}$  and 4 mM.<sup>49</sup>

Figure 5C compares the calculated CD and UV Raman temperature dependence of the AP  $\alpha$ -helical content. As discussed fully below, our CD calculation of the temperature dependence of the  $\alpha$ -helical content indicates a 55–60%  $\alpha$ -helix content at  $-4$  °C which decreases to zero by  $\sim 75$  °C. Also, as discussed below we calculate substantially more  $\alpha$ -helix content using our UV Raman methodology.

**Steady-State AP UV Resonance Raman Studies.** Figure 6 shows the static temperature dependence of the 204-nm UVRS of AP in water ( $\sim 15$  mg/mL). The spectra are dominated by the peptide linkage amide vibrational bands without any noticeable contribution from water. The high-temperature spectra ( $\sim 70$  °C) are dominated by the AmI ( $\sim 1658$   $\text{cm}^{-1}$ ), AmII ( $\sim 1547$   $\text{cm}^{-1}$ ),  $\text{C}_{\alpha}$ -H bending ( $\sim 1384$   $\text{cm}^{-1}$ ), and AmIII ( $\sim 1245$   $\text{cm}^{-1}$ ) bands. These AmI, AmII, and  $\text{C}_{\alpha}$ -H bending band frequencies are close to those observed for the average random coil conformations of proteins<sup>37</sup> (Table 1), while the AmIII band is downshifted by  $\sim 20$   $\text{cm}^{-1}$ . The three relatively weak bands at  $\sim 1452$ , 1166, and 1086  $\text{cm}^{-1}$  are at the correct frequencies to derive from the arginine side chain chromophores.<sup>37</sup> However, their Raman cross sections appear to be 3–5 times higher than that expected. The  $\sim 1456$   $\text{cm}^{-1}$  weak band also occurs in the UVRS of tri- and pentaalanine (vide infra).

The steady-state UVRS of AP change with temperature. At  $-5.5$  °C the spectra are consistent with a dominating  $\alpha$ -helical content whose abundance decreases as the temperature increases;<sup>54</sup> the  $\sim 1250$   $\text{cm}^{-1}$  random coil AmIII band has the lowest relative intensity at  $T = -5.5$  °C, while the maximum relative intensity is observed in the region of the  $\sim 1300$   $\text{cm}^{-1}$   $\alpha$ -helix AmIII band. The intensity of the random coil  $\sim 1382$   $\text{cm}^{-1}$  C–H sb band, which is weakest at  $T = -5.5$  °C, grows as the temperature increases. Only modest changes occur for the AmII band, which shows only small differences between the  $\alpha$ -helix and random coil forms, while the AmI band increases in frequency and broadens as AP melts to form the random coil.

(53) Quadrifoglio, F.; Urry, D. W. *J. Am. Chem. Soc.* **1968**, *90*, 2755–2760.

(54) Scholtz, J. M.; Qian, H.; York, E. J.; Stewart, J. M.; Baldwin, R. L. *Polymers* **1991**, *31*, 1463–1470.

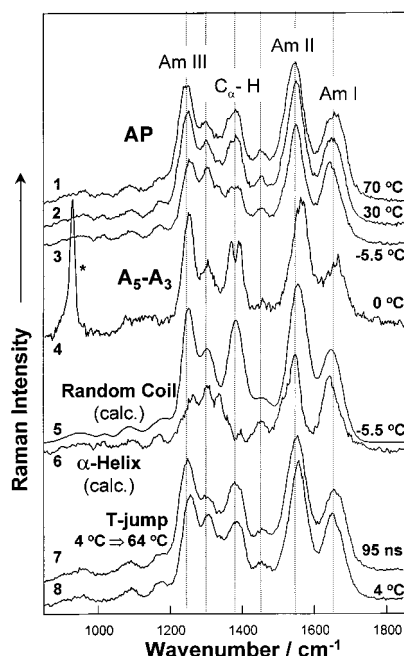


**Figure 6.** Comparison between steady-state and time-resolved 204-nm UVRS of AP ( $\sim 15$  mg/mL). AP UVRS measured at (1)  $+70$  °C, (2)  $+30$  °C, and (3)  $-5.5$  °C. (4) The  $0$  °C UV Raman difference spectrum between penta-Ala and tri-Ala; (5) pure random coil ( $T = -5.5$  °C); and (6)  $\alpha$ -helix ( $T = -5.5$  °C) basis Raman spectra of AP (see text). Transient UVRS of AP measured at (7) 95 ns after a T-jump of  $\sim 60$  °C and (8) a static UVRS of AP at  $4$  °C in the absence of a T-jump.

Attempts to utilize our previously determined protein basis spectra, obtained via pure secondary structure resonance Raman spectroscopy (PSSRS<sup>37</sup>), to model the temperature dependence of the AP secondary structure were not completely satisfactory, presumably because these “average spectra” are inhomogeneously broadened by a small side chain dependence of the band frequencies. The UVRS bands of AP are much narrower (vide infra). As demonstrated below, the AP random coil basis spectrum shows a significant temperature dependence of its intensity and frequency. Thus, we must carefully characterize these dependencies to accurately model the temperature dependence of the AP secondary structure.

**Temperature Dependence of Random Coil UVRS.** We can model the UVRS of random coil AP by characterizing the Raman spectra of the interior segments of small peptides which are too small to form  $\alpha$ -helices. The UVRS of small random coil peptides will differ from that of AP because of the larger relative contribution from the penultimate carboxylate and amine group in the small peptides. Previous studies<sup>55</sup> of isotopically substituted peptides demonstrated that *their UV Raman enhanced* amide vibrations are localized within each amide fragment. Thus, we should be able to subtract spectra of peptides of different lengths to obtain spectra of particular interior segments.

Figure 7 compares the 204-nm UV Raman  $80$  °C difference spectrum between pentaalanine ( $A_5$ ) and trialanine ( $A_3$ ) to the  $69$  °C spectrum of AP. The CD spectra of  $A_3$  and  $A_5$  indicate that they are both completely random coil (not shown), while the Figure 5A AP CD data clearly demonstrate that AP is completely random coil at this temperature. The  $A_3$  and  $A_5$  spectra show AmI, AmII, and AmIII bands at  $\sim 1660$ ,  $\sim 1550$ , and  $\sim 1245$   $\text{cm}^{-1}$ , respectively, while the C—H sb bending bands

occur at  $1381$   $\text{cm}^{-1}$ , and the symmetric  $\text{COO}^-$  stretching bands occur at  $\sim 1400$   $\text{cm}^{-1}$ . The difference spectrum, which models the internal two  $A_5$  amide linkages and avoids the contribution of the penultimate carboxylate and amine groups, is satisfyingly close to that of random coil AP which occurs at high temperatures.

Figure 8A shows the modeling of the  $A_5 - A_3$  difference spectrum to a minimum sum of mixed Gaussian–Lorentzian band shapes; the best fit was obtained when all the bands were Gaussian except those at  $\sim 1369$  and  $\sim 1394$  nm which were Lorentzian. The excellent fitting to the sum of mainly Gaussian band shapes, one for each observed band, gives us confidence in the underlying simplicity of the 204-nm excited UV Raman spectra, where we believe we have identified all of the underlying components.

We measured the temperature dependence of the random coil  $A_5 - A_3$  difference spectra in order to model the temperature dependence of the AP random coil basis spectra. Figure 9 shows that as previously observed for NMA, the frequencies mainly downshift and the bands broaden slightly.<sup>56</sup> It is evident from the low-temperature  $A_5 - A_3$  difference spectrum that the  $\text{C}\alpha\text{H}$  bending band consists of two narrow peaks at  $\sim 1369$  and  $\sim 1394$   $\text{cm}^{-1}$ , which become poorly resolved at higher temperatures.

As shown in Figures 9 and 10 and tabulated in Table 1, for temperatures between  $-5.5$  and  $80$  °C, the AmII ( $d\nu/dT = -0.15 \pm 0.02$   $\text{cm}^{-1}/^\circ\text{C}$ ) and AmIII ( $d\nu/dT = -0.10 \pm 0.02$   $\text{cm}^{-1}/^\circ\text{C}$ ) bands show the largest temperature dependencies, which are negative, while the AmI band shows a smaller positive slope ( $d\nu/dT = 0.08 \pm 0.01$   $\text{cm}^{-1}/^\circ\text{C}$ ). The other bands have much smaller negative slopes. These temperature-induced changes are also similar to that observed for pH 7 random coil polyglutamic acid (data not shown). In addition, Table 1 also displays the temperature slopes of the band peak height intensities and bandwidths obtained from spectral fitting to the best sum of Lorentzians and Gaussians by the use of the program Grams from Galactic Instruments.

The temperature dependence of the frequencies presumably results from anharmonic coupling to low-frequency modes, which when thermally populated decrease the bond force constants.<sup>56,57</sup> The AmII and AmIII bands are dominated by coupled C—N stretching and N—H bending motion. The N—H bending coordinate would be expected to be strongly coupled to numerous low-frequency amide group torsional motions. In contrast, the AmI band mainly derives from C=O stretching motion, which would be expected to be less coupled to low-frequency vibrations. The UVRS intensities decrease with temperature, despite the observed (Figure 4) increased 204 nm absorption and the apparent amide  $\pi \rightarrow \pi^*$  absorption redshift. These intensity decreases most likely result from a homogeneous line width increase for the resonant amide  $\pi \rightarrow \pi^*$  transition.

**Calculated AP Random Coil Basis Spectra.** We can use the observed  $70$  °C random coil AP spectrum and the measured temperature dependence of the  $A_3 - A_5$  UV resonance Raman difference spectra to model the AP random coil spectrum at any temperature. Since we see little temperature dependence of the  $A_5 - A_3$  difference spectral band shapes, we neglect band-shape changes. We can model the spectra by utilizing the linear temperature dependencies of the band frequencies,  $\nu_i^T$ , intensi-

(56) Song, S.; Asher, S. A.; Krimm, S.; Shaw, K. D. *J. Am. Chem. Soc.* **1991**, *113*, 1155–1163.

(57) (a) Harris, C. B.; Shelby, R. M.; Cornelius, P. A. *Phys. Rev. Lett.* **1977**, *38*, 1415. (b) Shelby, R. M.; Harris, C. B.; Cornelius, P. A. *J. Chem. Phys.* **1979**, *70*, 34. (c) Asher, S. A.; Murtaugh, J. *J. Am. Chem. Soc.* **1983**, *105*, 7244–7251.

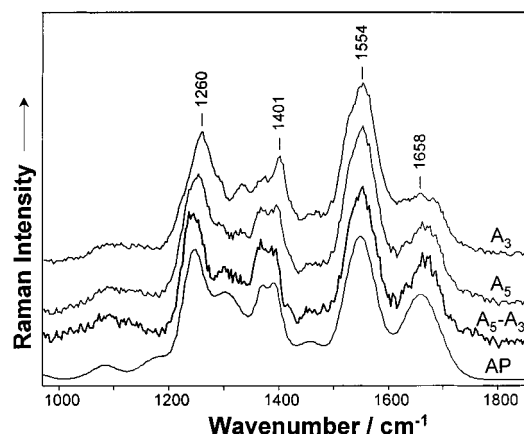
(55) Sieler, G.; Asher, S. A. Unpublished results.



**Table 1.** UV Raman Bands (cm<sup>-1</sup>) of AP (15 mg/mL), Trialanine, and Pentaalanine in Water and Their Temperature Dependences<sup>a</sup>

assignment	AP		A <sub>5</sub> - A <sub>3</sub> <sup>d</sup>				T <sub>room</sub>	
	70 °C	-5.5 °C	t <sub>room</sub>	dν/dT	dI/dT	dω/dT cm <sup>-1</sup> /°C	random coil <sup>b</sup>	α-helix <sup>b</sup>
Am I	1658	1643	1663	0.08 ± 0.01	-0.18	0.11	1665	1647
Am II	1547	1549	1560	-0.15 ± 0.02	-1.16	0.063	1560	1545
C <sub>α</sub> -H <sup>c</sup>	1384	1382	1369	-0.03 ± 0.01	-1.39	0.1	1386	none
	broad	broad	1394	-0.02 ± 0.01	-1.3	0.1		
Am III	1245	1254	1250	-0.10 ± 0.02	-1.59	0.07	1267	1299
? (A)	1303	1304	1303	-0.03 ± 0.02	-0.8	0.2		
? (A)		1355						
Arg	~1452	~1454	~1450				Arg <sup>37</sup>	
Arg	~1166	~1169					1454	
Arg	~1086	~1090					1176	
							1091	

<sup>a</sup> dν/dT, dI/dT, and dω/dT are the temperature dependence of frequency, intensity, and bandwidth, respectively, for the individual Raman bands (see text). <sup>b</sup> Amide bands in pure secondary structure Raman component spectra of proteins and polypeptides.<sup>37</sup> <sup>c</sup> Bending mode. <sup>d</sup> "Internal" residues of A<sub>5</sub> (see text); A, alanine; Arg, arginine.

**Figure 7.** Comparison between the 80 °C 204 nm UVRs of trialanine (A<sub>3</sub>, 1.5 mM) and pentaalanine (A<sub>5</sub>, 0.54 mM), their difference spectrum (A<sub>5</sub> - A<sub>3</sub>), and the UVRs of 69 °C random coil AP.

ties,  $I_i^T$ , and bandwidths,  $\omega_i^T$  given in Table 1:

$$\nu_i^T = \nu_i^0 + \frac{\partial \nu_i^T}{\partial T}(T - T_0) \quad (3a)$$

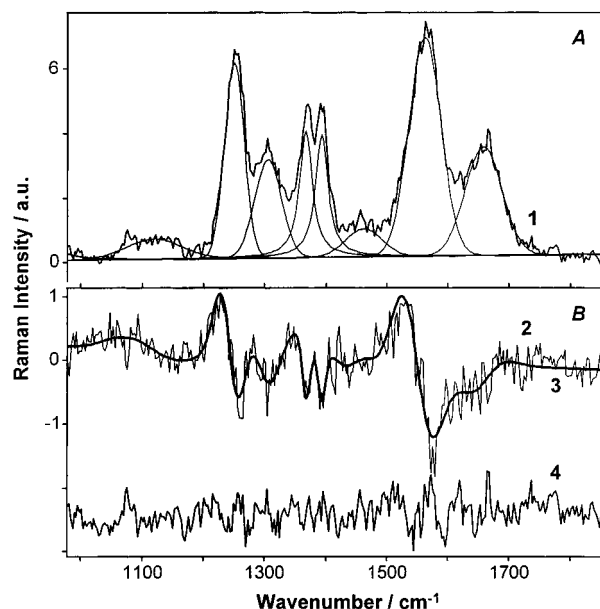
$$I_i^T = I_i^0 + \frac{\partial I_i^T}{\partial T}(T - T_0) \quad (3b)$$

$$\omega_i^T = \omega_i^0 + \frac{\partial \omega_i^T}{\partial T}(T - T_0) \quad (3c)$$

Where  $i$  designates the band,  $T$  is temperature, and  $T_0 = 70$  °C.

The CD measurements clearly indicate that AP is completely random coil at high temperatures. Thus, the high-temperature AP spectra (such as the  $T = 70$  °C AP spectra in Figures 6 and 7) can be utilized as pure random coil basis spectra to model the secondary structure composition. For lower temperatures we spectrally modeled the high-temperature AP UVRs with a minimum number of Gaussian-Lorentzian bands and calculated the random coil AP UVRs using eqs 3 and 4:

$$\sigma_r^T = \sum_i \left\{ g_i I_i^T \exp \left[ \frac{-(\nu_i^T - \nu)^2}{(\omega_i^T/0.59)^2} \right] + (1 - g_i) I_i^T \frac{(\omega_i^T/2)^2}{(\nu_i^T - \nu)^2 + (\omega_i^T/2)^2} \right\} \quad (4)$$

**Figure 8.** (A) Spectral modeling of the 0 °C A<sub>5</sub> - A<sub>3</sub> UVR difference spectrum decomposed into a minimum number of Gaussian and Lorentzian band shapes. The best fit for most bands was obtained by utilizing pure Gaussians. The only exceptions were the ~1369 and ~1394 cm<sup>-1</sup> bands which were pure Lorentzians. Part B shows (2) directly calculated 40 °C to 0 °C temperature difference spectrum between the A<sub>5</sub> - A<sub>3</sub> difference spectra; (3) calculated 40 °C to 0 °C temperature difference spectra between the spectrally modeled A<sub>5</sub> - A<sub>3</sub> difference spectra at 40 °C and 0 °C spectra; and (4) difference (residual) spectrum between the A<sub>5</sub> - A<sub>3</sub> UVR spectrum measured at 0 °C and the modeled spectrum. Note the lack of noise in the curve 3 modeled temperature difference spectrum compared to that using the actually measured spectra. Fitting the observed spectra to sums of bands whose bandwidths are constrained to be experimentally reasonable, effectively results in a realistic Fourier noise filtering of the observed spectra to result in much higher apparent S/N ratios. The random noise evident in curve 4, which shows the difference spectrum between the experimentally measured difference spectrum and that modeled, is indicative of a lack of bias for the modeling.

where  $g_i$  is the relative contribution of Gaussian to Lorentzian line shape for each single Raman band.

Figure 11A shows the accurate spectral modeling of the 69 °C AP random coil UVRs, while Figure 11B shows the resulting calculated temperature dependence of the random coil spectra. The fact that we can accurately model the 69 °C AP amide band UVRs with the same minimum number of bands as the A<sub>5</sub> - A<sub>3</sub> difference spectra encourages us in the modeling. As

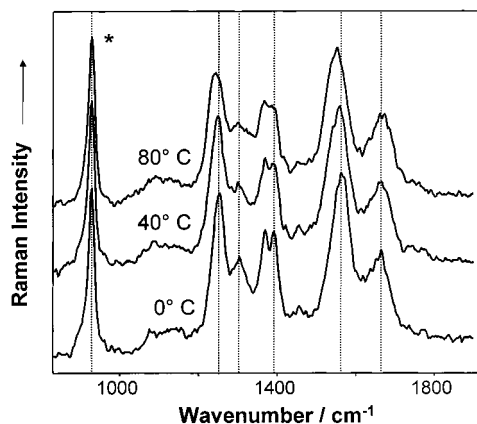


**Figure 9.** Temperature dependence of the 204-nm  $A_5 - A_3$  difference spectra. The spectra were normalized using the intensity of the 932  $\text{cm}^{-1}$  sodium perchlorate (0.2 M) internal standard band (\*).

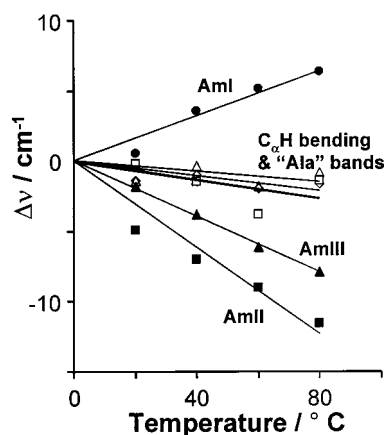


**Figure 10.** Temperature dependence of UVRS  $A_5 - A_3$  amide band frequencies obtained from measurements such as in Figure 9.

expected we see decreases in both frequencies and intensities of all, but the AmI band, which slightly increases in frequency and is almost invariant in intensity. In fact, the random coil AmI band is a good candidate for a temperature-independent internal intensity and frequency standard.

**Calculated AP  $\alpha$ -Helix Basis Spectra.** The pure secondary structure resonance Raman (PSSR) pure  $\alpha$ -helix and random coil protein spectra demonstrate that the  $\text{C}_\alpha\text{H}$  bending band occurs only in random coil and  $\beta$ -sheet peptides and no band maxima occur in this frequency region for the  $\alpha$ -helix conformation.<sup>37</sup> Thus, we can use the  $\text{C}_\alpha\text{H}$  bending band intensity at any temperature to determine the relative contribution  $(1 - f_\alpha)$  of the pure random coil AP spectrum, provided no  $\beta$ -sheet is present. Since the AP thermal transition occurs only between the  $\alpha$ -helix and random coil conformations, we can use eq 5 to calculate the AP  $\alpha$ -helix basis spectrum,  $S_\alpha(\nu)$ , from the observed AP spectrum,  $S_{\text{obs}}(\nu)$  at this temperature:

$$S_\alpha(\nu) = [S_{\text{obs}}(\nu) - S_r(\nu)(1 - f_\alpha)]/f_\alpha \quad (5)$$

Where  $f_\alpha$  is the fractional  $\alpha$ -helical composition. Figure 6 shows the calculated pure  $\alpha$ -helix UV resonance Raman basis spectrum of AP at  $T = -5.5^\circ\text{C}$ .

Figure 12A shows our modeling of the random coil spectral contribution to the spectra of AP from  $-7.4$  to  $69^\circ\text{C}$ . The calculated random coil basis spectrum is essentially identical to the AP spectra at high temperature. The observed spectra differ increasingly from that of the random coil spectrum for

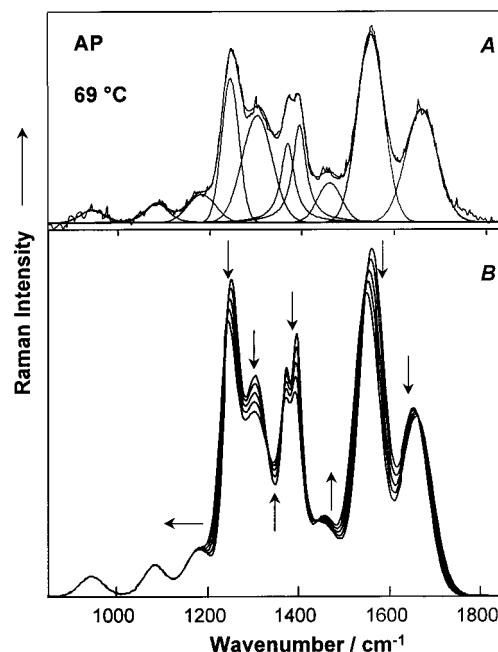


**Figure 11.** (A) Spectral modeling of  $69^\circ\text{C}$  204-nm AP (0.5 mg/mL) UVRS into a minimum number of Gaussian-Lorentzian; the best fit was obtained when all the bands were Gaussian except for the  $\sim 1369$  and  $\sim 1394 \text{ cm}^{-1}$  bands which were Lorentzians. (B) Calculated temperature dependence of the AP random coil spectra using eqs 3 and 4. Arrows indicate directions of changes due to temperature increases.

temperatures below  $30^\circ\text{C}$ , where the contributions from the  $\alpha$ -helix conformations become important and, in fact, dominate by  $10^\circ\text{C}$ .

**Modeling the Steady-State Temperature Dependence of AP Secondary Structure.** The calculated AP  $\alpha$ -helix and random coil spectra basis spectra shown in Figure 6 are similar to the PSSR  $\alpha$ -helix and random coil "average protein" spectra,<sup>37</sup> except that the AP basis spectra bands are narrower and their frequencies are shifted. For example, the AP AmIII random coil frequency region is resolved into a peak at 1250 and a shoulder at  $1300 \text{ cm}^{-1}$  compared to a single asymmetric broad band centered at  $1267 \text{ cm}^{-1}$  in the PSSR random coil spectrum. The AmIII band in the AP  $\alpha$ -helix basis spectrum is partially resolved into three components centered at  $\sim 1300 \text{ cm}^{-1}$  instead of the single  $\sim 1300 \text{ cm}^{-1}$  lump observed for the  $\alpha$ -helix PSSR spectra. The AmIII band cross section differences observed between the  $\alpha$ -helix and random coil AP basis spectra are essentially identical to those observed for the PSSR spectra. The same C-H sb band frequency of  $\sim 1382 \text{ cm}^{-1}$  is observed for random coil AP and the random coil PSSR spectra. The AP AmII random coil ( $1547 \text{ cm}^{-1}$ ) and the  $\alpha$ -helix ( $1554 \text{ cm}^{-1}$ ) basis spectra are narrower than those of the PSSR spectra. This narrowing is especially striking for the AP  $\alpha$ -helix  $1648 \text{ cm}^{-1}$  AmI band which occurs at the same frequency as that in the PSSR spectrum. The AP random coil  $1660 \text{ cm}^{-1}$  AmI is downshifted about  $5 \text{ cm}^{-1}$  from that of the PSSR spectra.

The AmI frequency upshift and broadening in the AP random coil basis spectrum, compared to that of the  $\alpha$ -helix, is similar to the previously observed AmI IR absorption band shift from  $1633$  to  $1665 \text{ cm}^{-1}$  due to  $\alpha$ -helix melting to random coil in a short alanine-arginine-based peptide of similar amino acid sequence to AP.<sup>23</sup> This shift to higher frequency was attributed both to the weaker hydrogen bonding to water compared to the intrahelix hydrogen bonding and to changes in the AmI vibrational coupling. The broadening of the AmI band was



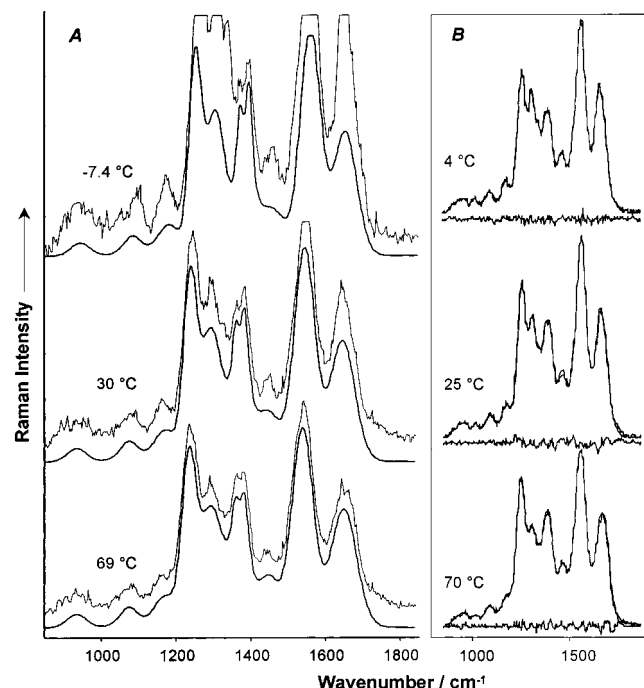


**Figure 12.** (A) Comparison between the observed temperature dependence of the 204-nm UVRs of AP (0.5 mg/mL) and modeled spectra, where temperature-dependent random coil spectra from Figure 11 are used to model the intensities in the C–H bending band region. The modeled pure random coil spectra are moved down for clarity. (B) Modeling the steady-state temperature dependence of the observed 204-nm AP (15 mg/mL) UVRs using eq 6, and the temperature-dependent random coil basis spectra of Figure 11 and the assumed temperature independent  $\alpha$ -helix basis spectrum shown in Figure 6. The excellence of the modeling is shown by the small residuals which result from subtraction of the calculated spectra from those observed.

attributed to an increased inhomogeneous broadening due to an increased distribution of peptide random coil conformers.<sup>23</sup>

We can use the temperature-dependent AP pure random coil spectra shown in Figure 11 and the  $T = -5.5$  °C  $\alpha$ -helix basis spectrum of Figure 6, curve 6 to calculate the fractional  $\alpha$ -helix conformation,  $f_\alpha$  for each observed AP spectra at each temperature. We modeled the observed spectra by using eq 6 through a nonlinear least-squares best fit of the basis spectra:

$$\sigma_{\text{obs}}^T(\nu) \cong \sigma_\alpha(\nu)f_\alpha + \sigma_r^T(\nu)(1 - f_\alpha) \quad (6)$$

where  $\sigma_{\text{obs}}^T(\nu)$  are the observed 204-nm UVRs cross sections at Raman frequencies  $\nu$  at temperature  $T$ , and  $\sigma_\alpha(\nu)$  and  $\sigma_r^T(\nu)$  are the basis spectra Raman cross sections. We note that at this point we approximate  $\sigma_\alpha(\nu)$  to be temperature independent.

The excellence of this modeling approach is clearly seen in Figure 12B which compares the modeled to the observed spectra; the small residuals indicate that over the temperature region of significant  $\alpha$ -helix abundance little change occurs in the  $\alpha$ -helix basis spectra. The residual spectra mainly show high-frequency noise. This is another indication that a two-state  $\alpha$ -helix to random coil model adequately describes the AP  $\alpha$ -helix  $\rightarrow$  random coil thermal transition.

Figure 5C shows the temperature dependence of the  $\alpha$ -helix fractional abundance calculated from the AP UVRs for AP concentrations of 0.5 and 15 mg/mL. The estimated  $f_\alpha$  values are essentially identical for the two concentrations and indicate a decrease in the  $\alpha$ -helical content from  $\sim 63\%$  at  $-4$  °C to 0% by 70 °C.

**CD and UVRs Display Different AP Secondary Structure Temperature Dependences.** The UVRs-calculated  $\alpha$ -helix content significantly differs from that calculated from the CD spectra. This results from differences in the physical basis of the spectroscopies. CD secondary structure determination in our case only monitors the  $\alpha$ -helix since the random coil gives a negligible spectral contribution. In contrast, the UVRs, which monitors both the random coil and  $\alpha$ -helix spectral signatures, should better determine secondary structure.

CD is expected to more heavily weight longer  $\alpha$ -helices.<sup>58,59</sup> This may explain why we calculate similar  $\alpha$ -helical contents with CD and UVRs at low temperatures where the helices are abundant and long. In contrast, at higher temperatures the CD may underestimate the  $\alpha$ -helix content because it fails to detect shorter  $\alpha$ -helices. We will discuss detailed comparisons of CD and UVRs secondary structure determinations in a future publication.

**Steady-State Random Coil  $\rightarrow$   $\alpha$ -Helix Transition Thermodynamics.** The thermodynamics of polypeptides and protein helix  $\rightarrow$  random coil transitions have been extensively studied both theoretically and experimentally.<sup>54,60</sup> Special attention has been paid to A-oligopeptides which form  $\alpha$ -helical structures in aqueous solution at low temperatures.<sup>59,61–63</sup> IR spectroscopy shows that these A-oligopeptides unfold to the random coil on the same time scale as the  $\alpha$ -helix conformation is depleted.<sup>23</sup> High-resolution NMR measurements reveal that these peptides fold into a mixture of  $\alpha$ -helix and  $3_{10}$ -helix,<sup>64</sup> while recent VCD studies of A-rich peptides suggest that  $3_{10}$ -helical structures form the junctions between  $\alpha$ -helix and random coil segments.<sup>59</sup>

Our CD and the UVRs results can be used to independently determine the thermodynamics of the  $\alpha$ -helix  $\rightarrow$  random coil transition by applying the standard two-state model<sup>65</sup> and by assuming that  $\Delta C_p = 0$ . We assume that the standard enthalpy,  $\Delta H$ , and entropy changes,  $\Delta S$ , are independent of temperature.

**CD-Determined Thermodynamic Parameters.** The temperature dependence of the equilibrium constant,  $K$ , for the random coil  $\leftrightarrow$  helix equilibrium can be modeled using eq 7. This empirical modeling of the thermodynamic parameters is independent of the values of  $k$  and  $[\theta]_\infty$ .

$$K = \exp(-\Delta H/RT + \Delta S/R) = ([\theta] - [\theta]_r)/([\theta]_\alpha - [\theta]) \quad (7)$$

where  $R$  and  $[\theta]$  are the gas constant and the 222-nm AP mean residue molar ellipticities observed at temperature  $T$ , while  $[\theta]_\alpha$  is the limiting ellipticity at low temperature determined from TFE experiments, and  $[\theta]_r$  is the 222-nm mean residue molar ellipticity for 100% random coil AP at high temperature.

Curve 1 of Figure 5B shows the least squares best fit of eq 7 to the CD melting data which yields  $R^2 > 0.999$ . The

(58) Fasman, G. D., Ed. *Circular Dichroism and the Conformational Analysis of Biomolecules*; Plenum Press: New York, 1996.

(59) Yoder, G.; Pancoska, P.; Keiderling, T. A. *Biochemistry* **1997**, *36*, 15123–15133.

(60) (a) Gruenewald, B.; Nicola, C. U.; Lustig, A.; Schwarz, G.; Klump, H. *Biophys. Chem.* **1979**, *9*, 137–147, and references therein. (b) Scholtz, J. M.; Baldwin, R. L. *Annu. Rev. Biophys. Biomol. Struct.* **1992**, *21*, 95–118. (c) Guo, Z.; Thirumalai, D. *J. Mol. Biol.* **1996**, *263*, 323–343.

(61) Scholtz, J. M.; Barrick, D.; York, E. J.; Stewart, J. M.; Baldwin, R. L. *Proc. Natl. Acad. Sci. U.S.A.* **1995**, *92*, 185–189.

(62) Ooi, T.; Oobatake, M. *Proc. Natl. Acad. Sci. U.S.A.* **1991**, *88*, 2859–2863.

(63) Scholtz, J. M.; Marqusee, S.; Baldwin, R. L.; York, E. J.; Stewart, J. M.; Santoro, M.; Bolen, D. W. *Proc. Natl. Acad. Sci. U.S.A.* **1991**, *88*, 2854–2858.

(64) Millhauser, G. L.; Stenland, C. J.; Hanson, P.; Bolin, K. A.; van-de-Ven, F. J. M. *J. Mol. Biol.* **1997**, *267*, 963–974, and references therein.

(65) Becktel, W. J.; Schellman, J. A. *Biopolymers* **1987**, *26*, 1859–1877, and references therein.

**Table 2.** Thermodynamic Parameters for AP Coil–Helix Transition

	AP concentration	$\Delta H$ , kcal/mol	$\Delta S$ , cal/(mol K)	$f_{\text{end}}$
CD	0.5–15 mg/mL	$-12.1 \pm 1$	$-43.2 \pm 4$	
UVRS	15 mg/mL	$-11 \pm 3$	$-37 \pm 9$	$0.32 \pm 0.1$
UVRS	0.5 mg/mL	$-12 \pm 2$	$-41 \pm 7$	$0.29 \pm 0.06$
IR <sup>a</sup>	2 mM	$-12 \pm 2$	$-36 \pm 6$	

<sup>a</sup> The two-state model applied to the temperature dependence of the AmI' IR band of 21 residue A-based peptide, Suc-A<sub>5</sub>-(A<sub>3</sub>RA)<sub>3</sub>-A-NH<sub>2</sub> (Suc = succinyl), in D<sub>2</sub>O.<sup>23</sup>

thermodynamic parameters are listed in Table 2 along with the standard errors ( $\pm 2\sigma$ ). We calculate that  $\Delta H = -12.1$  kcal/mol, which results in a mean  $\Delta H$  value per residue of  $-0.77$  kcal/mol, if we exclude the typical 4.3 terminal residues which cannot effectively fully form  $\alpha$ -helix structures<sup>44</sup> (vide infra). Previous CD and calorimetric studies found  $\Delta H$  values per residue of  $\sim -1$  kcal/mol both for ionizable polypeptides<sup>66,67</sup> (after correction for the heat of ionization of the side chains) and for A-oligopeptides.<sup>54,63</sup> Our calculated entropy of folding per residue,  $\Delta S = -2.8$  cal/(mol deg) is close to the  $-3.4$  cal/(mol deg) value reported for polyglutamic acid.<sup>67</sup>

$\Delta C_p$  has been found to be negative and of significant value for several proteins,<sup>65</sup> due to hydrophobic effects such as the transfer of nonpolar side chains from water to the nonpolar protein interior.<sup>68</sup> However, our  $\Delta C_p = 0$  assumption used here, for AP should still be appropriate, because of the small ala side chain surface water accessibility<sup>69</sup> and because the ala amino acid side chains are too short for significant intramolecular side-chain hydrophobic interactions within the  $\alpha$ -helix.

Our uncertainties in the exact  $k$  and  $[\theta]_\infty$  values result in corresponding uncertainties in the CD determination of the  $\alpha$ -helical fraction. Curves 1 and 2 of Figure 5C represent two limiting cases: curve 1 was calculated by using  $k = 4.3$  and  $[\theta]_\infty = -32\,245$  (deg cm<sup>2</sup>)/dmol, while curve 2 utilized  $k = 7.6$  and  $[\theta]_\infty = -40\,000$  (deg cm<sup>2</sup>)/dmol. Thus, our CD results indicate that at  $-5$  °C AP in aqueous solution is between 50 and 64%  $\alpha$ -helical, and that AP is negligibly  $\alpha$ -helical by 50 °C.

**UV Raman-Determined Thermodynamic Parameters.** We can use our UV Raman determination of the temperature dependence of the AP  $\alpha$ -helix content and eq 8 to also determine the thermodynamic parameters associated with the random coil  $\leftrightarrow$  helix equilibrium.

$$f_\alpha = \frac{1 - f_{\text{end}}}{1 + \exp\left(-\left(\frac{\Delta H}{RT} - \frac{\Delta S}{R}\right)\right)} \quad (8)$$

Where  $f_{\text{end}}$  is the terminal residue fraction remaining unordered at low temperatures. We obtain thermodynamic parameters very close to that determined from our modeling of the CD spectra (Table 2).  $f_{\text{end}}$  was calculated to be  $0.3 \pm 0.05$ , which corresponds to a value of  $k = 6$  in eq 2b.

The terminal amide groups of a peptide can only form one internal hydrogen bond instead of the two hydrogen bonds of the central  $\alpha$ -helix amide groups. Consequently, these residues may not overcome the entropy change associated with  $\alpha$ -helix formation and may remain unordered at low temperatures.

(66) (a) Chou, P. Y.; Scheraga, H. A. *Biopolymers* **1971**, *10*, 657–680. (b) Rialdi, G.; Hermans, J. J. *J. Am. Chem. Soc.* **1966**, *88*, 5719–5720.

(67) Hermans, J. J. *J. Phys. Chem.* **1966**, *70*, 510–515.

(68) (a) Spolar, R. S.; Record, M. T. *J. Science* **1994**, *263*, 777–784. (b) Dill, K. A. *Biochemistry* **1990**, *29*, 7133–7155.

(69) Richards, F. M. *Annu. Rev. Biophys. Bioeng.* **1977**, *6*, 151–176.

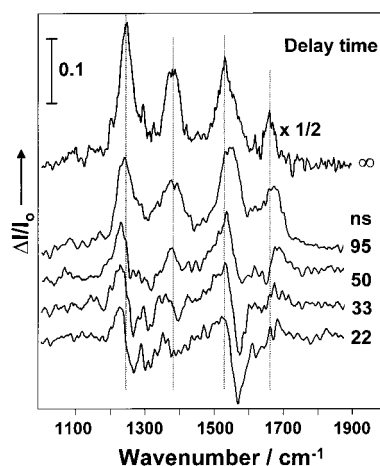


**Figure 13.** Temperature jump difference UVRS of AP at different delay times between pump and probe. The top infinite delay time spectrum is a static difference UVRS of AP measured at 37 and 4 °C. This static difference spectrum is identical to that of the transient difference spectrum measured at an infinite delay time. Transient difference UVRS of AP initially at 4 °C were measured 22, 33, 50, and 95 ns after a  $T$ -jump of  $\sim 33^\circ$ . The static UVRS of AP at 4 °C is subtracted from each of the transient spectra and the difference spectra are ratioed to the maximum AmII band intensity in the static 4 °C AP UVRS. The transient difference spectra were Fourier-smoothed (40% smoothing degree).

Fluorescence probe studies have shown significantly smaller  $\alpha$ -helical abundances for the terminal residues of A peptides.<sup>19</sup>

Our UV Raman results calculate a significantly larger fraction  $\alpha$ -helical content than is calculated from our CD results (Figure 5C). As will be discussed more fully in a subsequent publication, we believe that this mainly results from a bias of the CD ellipticity per residue values against short  $\alpha$ -helical segments. This gives rise to a decreased estimate of the  $\alpha$ -helical content at higher temperatures where the helices are shorter. This also accounts for the closer Raman and CD calculated  $f_\alpha$  values at the lower temperatures.

**Time-Resolved UVRS Nanosecond  $T$ -Jump Dynamics.** We measured nanosecond transient UVRS of aqueous AP solutions initially at 4 °C by inducing  $T$ -jumps of between 30 and 65 °C with our 1.9- $\mu$ m IR pump beam. We then probed the sample with 204-nm UVRS probe pulses at delay times between 22 and 95 ns. Figure 6, curve 7 shows a transient resonance Raman spectrum of AP measured 95 ns after  $T$ -jump of  $\sim 65$  °C, compared to a 4 °C spectrum measured in the absence of the pump beam (curve 8). The  $T$ -jump at the longest time delays results in spectral changes similar to those observed by heating the sample (Figure 6, curves 1–3); intensity increases most visibly occur for the random coil AmIII and C–H sb bands at 1244 and 1382 cm<sup>-1</sup>.

Figure 13 shows a series of difference spectra obtained by subtracting the “cold” equilibrium spectrum measured at 4 °C from the “hot” transient spectra measured at different delay times after a  $\sim 33$  °C  $T$ -jump. Each of the difference spectra was normalized to the intensity of the cold equilibrium spectrum AmII band.

Figure 13 shows a 37 °C – 4 °C difference spectrum between static 37 °C and 4 °C equilibria spectra. This difference spectrum corresponds to the transient  $T$ -jump spectrum with an infinite delay time for the probe pulse. The spectral differences observed here result from a decrease from  $\sim 52\%$   $\alpha$ -helix at 4 °C to 20%  $\alpha$ -helix content at 37 °C.

The relative difference spectrum at the 95-ns delay closely resembles this infinite delay time spectrum, but the relative

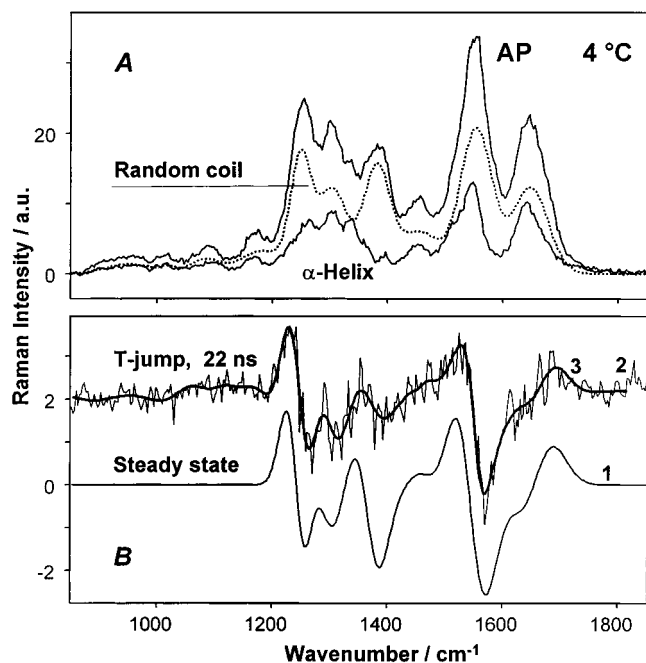


**Figure 14.** (A) Deconvolution of the 4 °C 204-nm AP (15 mg/mL) UVRS into its underlying  $\alpha$ -helix and random coil basis spectral contributions. (B) Curve 1: UVRS temperature difference spectrum between a modeled 37 °C spectrum where AP has the secondary structure composition at 4 °C and the observed 4 °C AP spectrum. Curve 2: Transient AP  $T$ -jump UV resonance Raman difference spectrum obtained by subtracting a 4 °C steady-state Raman spectrum from the spectrum measured 22 ns after a  $\sim 33$  °C  $T$ -jump (from Figure 14). Curve 3: This smooth curve, which does not have the noise of the directly subtracted experimental data of curve 1, was obtained by subtracting modeled curve fit spectra. This effectively improves the spectral S/N (see text).

intensities are between 2- and 3-fold smaller, and the bands are somewhat broadened. Thus, the  $\alpha$ -helix unfolding is still incomplete 95 ns after the  $T$ -jump (to between 36% and 42%  $\alpha$ -helix). At 50-ns delay, the difference features are still weaker, but still resemble the infinite delay time spectra. The spectral features diagnostic of  $\alpha$ -helix melting are not observed for 22- or 33-ns delays; instead other difference features occur.

These short delay time difference spectral features do not signal significant conformational changes, but instead merely result from temperature-dependent band shifts. For example, Figure 8 shows that the  $A_5 - A_3$  40 °C  $- 0$  °C temperature difference spectrum closely resembles the 22- and 33-ns delay time difference spectra of Figure 13. The major changes due to the  $T$ -jump occur for the AmII and AmIII bands at short delay times. Since no changes in conformation have occurred for the  $A_5 - A_3$  spectra, the temperature dependence results entirely from the temperature dependencies of the Raman band intensities and frequencies.

Figure 14A shows the 4 °C static AP spectrum deconvoluted into its component  $\alpha$ -helix and random coil contributions. We used the temperature dependence of the random coil basis spectra to calculate the AP difference spectrum between 37 and 4 °C, for the situation that the 37 °C fractional  $\alpha$ -helix composition remains identical to that at 4 °C. Figure 14B compares this modeled difference spectrum (curve 1) to the observed 22-ns transient difference spectrum (curves 2 and 3). Obviously, the 22-ns observed transient features derive mainly from the  $T$ -jump. Thus, we can reliably conclude that the spectral changes prior to 50-ns are mainly indicative of temperature alterations. At the same time, the discrepancy between spectra

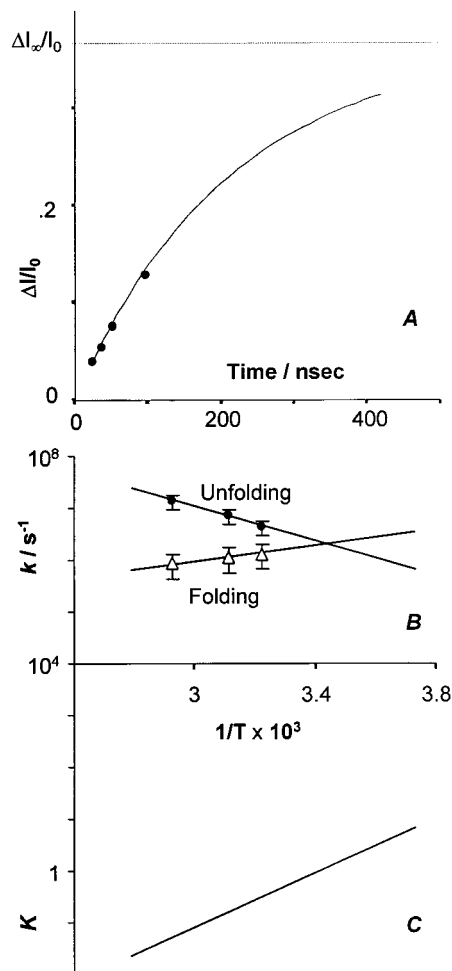


**Figure 15.** (A) UVRS measured kinetics of AP thermal denaturation. The ordinate is the relative change in the Raman intensity at  $1236\text{ cm}^{-1}$  obtained from the transient difference UVRS of Figure 14. Temperature dependence of (B) the AP folding and unfolding rate constants and (C) the  $\alpha$ -helix  $\rightleftharpoons$  random coil equilibrium constant.  $K$  was calculated from the Raman data.

1 and 3 (Figure 14B) especially, in the region of the  $\sim 1400\text{ cm}^{-1}$   $C_{\alpha}H$  bending mode, indicates that some AP secondary structural alterations have occurred even at the shortest tested delay times.

Figure 15A displays the kinetics of the relaxation phenomena associated with the 33 °C  $T$ -jump as measured by the magnitude of the maximum relative difference spectral feature at  $1233\text{ cm}^{-1}$  measured at different delay times (data extracted from the difference spectra of Figure 13). The value at the infinite delay time was determined from the static difference spectrum obtained from equilibrium measurements. The spectral relaxation time for the  $T$ -jump was estimated assuming monoexponential kinetics. For this 33 °C  $T$ -jump we obtain a 210-ns relaxation time for the  $1233\text{ cm}^{-1}$  band (Figure 15A) and a  $180 \pm 60$  ns average relaxation time using all four peaks of the Figure 13 difference spectra. We similarly measured the relaxation times for  $T$ -jumps of 43 and 65 °C, which gave times of  $120 \pm 50$  and  $70 \pm 30$  ns, respectively.

## Discussion

**Kinetics of Random Coil  $\rightarrow$   $\alpha$ -Helix Transition.** Monoexponential relaxation kinetics must occur for any simple two-state system. However, monoexponential relaxation is often also observed for more complex systems that dynamically partition



**Table 3.** Kinetic Parameters for AP  $\alpha$ -Helix  $\rightarrow$  Random Coil Thermal Transition

	$T, ^\circ\text{C}$			$E_a (\Delta H^\circ),$ kcal/mol
	37	48	64	
$\tau_{\text{rel}}, \text{ns}$	$180 \pm 60$	$120 \pm 50$	$70 \pm 30$	
$K$				
Raman <sup>a</sup>	0.31	0.16	0.07	$-12 \pm 2$
CD <sup>b</sup>	0.14	0.062	0.016	$-12 \pm 2$
$\tau_{\text{r}}, \text{ns}$				
Raman <sup>a</sup>	$240 \pm 60$	$140 \pm 50$	$75 \pm 30$	8
CD <sup>b</sup>	210	130	70	$7 \pm 2$
$\tau_{\alpha}, \mu\text{s}$				
Raman <sup>a</sup>	$0.76 \pm 0.4$	$0.87 \pm 0.5$	$1.1 \pm 0.6$	$-4^{+3}_{-2}$
CD <sup>b</sup>	$1.1^{+1}_{-0.3}$	-	-	$-7 \pm 3$

<sup>a,b</sup> Kinetic parameters were calculated using the thermodynamic parameters,  $K$ ,  $\Delta H$ , and  $\Delta S$ , determined from (a) Raman or (b) CD<sup>35</sup> measurements.

into two-state systems. For example, the recent energy landscape and the protein folding funnel theories predict monoexponential relaxation even in the presence of complex energy landscapes. Thus, we begin our analysis of the peptide unfolding kinetics by assuming monoexponential decay for our AP  $\alpha$ -helix  $\rightarrow$  random coil  $T$ -jump relaxation. Because 95 ns is the longest delay time possible in our single laser  $T$ -jump experiment, we are as yet unable to experimentally verify that the relaxation is monoexponential out to long delay times. However, we will soon complete construction of an independent  $T$ -jump transient UV resonance Raman spectrometer which will permit any delay time desired. This will allow us to directly determine whether the decay is truly monoexponential.

Previous  $T$ -jump unfolding studies of an  $\alpha$ -helical A peptide<sup>23</sup> demonstrated that unfolding to the random coil occurs during the time interval of  $\alpha$ -helix depletion. This is consistent with our results and further justifies our use of a two-state model (random coil  $\rightleftharpoons \alpha$ -helix) to interpret the kinetic data. In this case the relaxation kinetics are determined by the sum of the rate constants,  $k_{\alpha}$  and  $k_r$ , for the formation and the melting of  $\alpha$ -helices. The ratio of these rate constants determines the equilibrium constant,  $K = k_{\alpha}/k_r$ , which we independently determined from the steady-state UVRS measurements of  $f_{\alpha}$  (eq 6). Thus, we calculate reciprocals of the  $\alpha$ -helix melting rate constants of  $240 \pm 60$ ,  $140 \pm 50$ , and  $75 \pm 30$  ns at 37, 48, and 69  $^\circ\text{C}$ , respectively. Our value of the reciprocal of the  $\alpha$ -helix formation rate constant is  $\sim 0.8 \mu\text{s}$  at 37  $^\circ\text{C}$ . The increased uncertainties in the reciprocals of the  $\alpha$ -helix formation rate constants result from the rather small contributions that the  $\alpha$ -helix formation rate constant makes to the overall  $T$ -jump relaxation rate at this temperature.

A plot of the temperature dependence of the  $\alpha$ -helix melting rate constants demonstrates that they show Arrhenius-type behavior with an  $8 \pm 2$  kcal/mol activation energy (Figure 15B). Assuming our two-state model, we can then calculate the temperature dependence of the  $\alpha$ -helix formation rate constants:  $k_{\alpha} = K k_r$  (Figure 15B). In contrast, to the rate constant for unfolding, the folding rate constant,  $k_{\alpha}$  decreases as the temperature increases to give an anti-Arrhenius negative activation energy of  $-4^{+3}_{-2}$  kcal/mol (Figure 15B, Table 3).<sup>70</sup> This result clearly indicates the failure of transition state theory in this simple two-state modeling of AP thermal unfolding, which assumes a temperature-independent potential energy profile

(70) The value of  $-4^{+3}_{-2}$  kcal/mol for the apparent activation energy for AP  $\alpha$ -helix formation differs slightly from the value of  $-7 \pm 3$  kcal/mol reported in our preliminary Communication.<sup>35</sup> The difference derives from the more sophisticated spectral analysis approach used here to characterize the AP secondary structural composition.

along the reaction coordinate. This behavior could occur if the energy surfaces are temperature-dependent. This of course leads to a much more complex model which is not strictly two-state.

Our measured 37  $^\circ\text{C}$  180-ns relaxation time is very close to the 27.4  $^\circ\text{C}$  160-ns relaxation time measured for a similar short peptide using IR  $T$ -jump spectroscopy.<sup>23</sup> However, our calculated  $k_h$  and  $k_c$  values differ from those experimentally determined by recent  $T$ -jump IR measurements for this similar 21 amino acid residue A-peptide,<sup>23</sup> because our UVRS determined static secondary-structure compositions differ considerably from those they reported. The source of this discrepancy may result from their less accurate IR composition measurements. Our UVRS measured compositions are also similar to those of an A peptide studied in ref 19. Our rates are also close to those theoretically calculated using a zipper model<sup>19</sup> for this short A-based peptide.

Our value of  $\sim 0.8 \mu\text{s}$  for the reciprocal of the  $\alpha$ -helix formation rate constant is close to previous estimates of the upper rate limit for protein folding,<sup>15</sup> but is somewhat smaller than the 6  $\mu\text{s}$  value observed for a  $\beta$ -hairpin folding of a 16 amino acid residues.<sup>18</sup> In fact, a weak anti-Arrhenius behavior ( $E_a = -1$  kcal/mol) was recently observed in fluorescence spectral  $T$ -jump studies of a model  $\beta$ -hairpin peptide.<sup>17,18</sup>

Complex (non-Arrhenius) protein folding temperature dependencies have previously been observed.<sup>71,72</sup> These behaviors were proposed to result either from a super-Arrhenius reaction temperature dependence on a rough energy landscape, or to result from an unusual temperature dependence of hydrophobic interactions.<sup>71</sup> The "zipper" model,<sup>73</sup> which appears to accurately describe folding kinetics of short peptides, predicts complex temperature dependences for folding.<sup>19</sup> In agreement with this model, we observe that the rate constant for folding of the random coil to the  $\alpha$ -helix decreases as the temperature increases, while the helix  $\rightarrow$  random coil unfolding rate constant increases with temperature.

The relaxation rate for the random coil  $\rightleftharpoons \alpha$ -helix equilibrium is determined by the faster of the random coil  $\rightarrow \alpha$ -helix and  $\alpha$ -helix  $\rightarrow$  random coil reaction rates. The relaxation rates should exhibit a minimum at the midpoint of the folding curve.<sup>7,12,19</sup> The energy landscape theory similarly predicts an increase in the relaxation rates at low and high temperatures.<sup>9</sup> Dill et al.'s<sup>7,8</sup> recent 2D lattice model predicts Arrhenius behavior for protein unfolding and an anti-Arrhenius behavior (negative apparent activation energy) for protein folding around the heat denaturation region. This is in good qualitative agreement with our measured temperature dependence of the  $\alpha$ -helix formation and melting rate constants.

The competition between the energy bias toward the native conformation and the landscape roughness determines the detailed folding mechanism.<sup>9</sup> Thus, the folding kinetics depends on whether local or nonlocal interactions dominate the folding dynamics.<sup>74</sup> Fast protein folding events would occur in the presence of a dominating energy bias toward the native state, where the roughness of the landscape does not significantly impede progress toward the native state conformation.<sup>11</sup> Slower

(71) Scalley, M. L.; Baker, D. *Proc. Natl. Acad. Sci. U.S.A.* **1997**, *94*, 10636–10640, and references therein.

(72) (a) Tan, Y.-J.; Oliveberg, M.; Fersht, A. R. *J. Mol. Biol.* **1996**, *264*, 377–389. (b) Schindler, T.; Schmid, F. X. *Biochemistry* **1996**, *35*, 5; 16833–16842. (c) Alexander, P.; Orban, J.; Bryan, P. *Biochemistry* **1992**, *31*, 7243–7248.

(73) Cantor, C. R.; Schimmel, P. R. *The Behaviour of Biological Macromolecules*; Biophysical Chemistry; W. H. Freeman: San Francisco, 1980; Part III.

(74) Dill, K. A.; Bromberg, S.; Yue, K.; Fiebig, K. M.; Yee, D. P.; Thomas, P. D.; Chan, H. S. *Protein Sci.* **1995**, *4*, 561–602.

folding processes often result from the formation of a energy landscape bottleneck in folding which slows progress toward the native state.<sup>10,11,32,75</sup> Although multiple configurations may simultaneously be involved in the effective bottleneck state, the multiple configuration kinetics can average out to result in a simple folding behavior.<sup>11</sup> In this case the occurrence of a single effective thermodynamic barrier separating the folded and unfolded states gives rise to an "effective" two-state system with monoexponential relaxation kinetics, as has been reported for several proteins<sup>15,22,30,31</sup> and short peptides.<sup>17–19</sup>

It is important to note, however, that biexponential relaxation kinetics have been observed for a similar short A-based peptide using a nanosecond *T*-jump and followed by time-resolved IR absorption measurements.<sup>23</sup> The origin of the faster 10-ns relaxation time component of the biexponential decay is still controversial. One interpretation attributes the faster component to a temperature-induced IR spectral shift which is not correlated with secondary structure changes.<sup>23</sup> Alternatively, this fast component could result from the melting of terminal  $\alpha$ -helices.<sup>19,76</sup> Very fast ( $\sim 1$  ns) nonexponential relaxation was also observed in the *T*-jump studies of ribonuclease A  $\beta$ -sheet melting.<sup>24</sup> Hochstrasser and co-workers argued that particular intermediates must form in order to destabilize the  $\beta$ -sheet structure; the formation of these intermediates are involved in the fast kinetics, while melting of these intermediates occurs for the longer time relaxation.<sup>24</sup>

## Conclusions

We have demonstrated the utility of UV resonance Raman spectroscopy to probe the earliest events of the thermal unfolding of an  $\alpha$ -helical peptide. We find that the unfolding rate constant of  $(240 \text{ ns})^{-1}$  at  $37^\circ\text{C}$  shows Arrhenius behavior by increasing with temperature with an apparent activation barrier of 8 kcal/

mol. In contrast, the folding rate constant of  $(0.8 \mu\text{s})^{-1}$  shows anti-Arrhenius behavior and decreases with temperature with an apparent activation barrier of  $-4$  kcal/mol.

We believe that these results, which are the first measurements of activation barriers for the earliest stages in  $\alpha$ -helical peptide or protein folding and unfolding, are clear experimental indicators of the complexity of the peptide folding mechanism. Although monoexponential relaxation is expected for simple systems, macromolecules utilize much more complex multidimensional reaction coordinates. This concept has recently been emphasized by the proposed energy landscape and protein folding funnel theories which propose that the folding and unfolding rates are determined by the competition between the landscape energy surface slope and the landscape roughness along the paths connecting the native and unfolded protein structures.<sup>3,4</sup> Obviously, our temperature-dependent rate constants are sensing this energy landscape complexity at the earliest stages of folding and unfolding. The slower folding kinetics and their unusual temperature dependence signals a folding bottleneck which may involve  $\alpha$ -helix nucleation.

We believe that our nanosecond UVRS *T*-jump methodology has a unique ability to probe the complexity of the energy landscape. In the future we will isotopically substitute along the amide chains to separately examine the secondary structural evolution of different parts of the reaction coordinate space. For other peptides and proteins we can selectively monitor the environments of aromatic amino acids with  $\sim 230$  nm excitation to examine additional portions of the reaction surface. These experiments are now underway.

**Acknowledgment.** We gratefully acknowledge Dr. C. H. Munro for his valuable technical advice and NIH grant GM30741 for financial support.

JA991382F

(75) Shakhnovich, E. I. *Curr. Opin. Struct. Biol.* **1997**, *7*, 29–40.

(76) Dyer, R. B. Private communication.